Available online at www.sciencedirect.com
ScienceDirect
Journal of Sound and Vibration 300 (2007) 88–100
JOURNAL OF SOUND AND VIBRATION
www.elsevier.com/locate/jsvi

Wave propagation modelling in 1D structures using spectral finite elements

P. Kudela[a,*], M. Krawczuk[a,b], W. Ostachowicz[a,c]

[a]*Institute of Fluid Flow Machinery, Polish Academy of Sciences, ul. Fiszera 14, 80-952 Gdansk, Poland*
[b]*Faculty of Electrical and Control Engineering, Technical University of Gdansk, Narutowicza 11/12, 80-952 Gdansk, Poland*
[c]*Gdynia Maritime University, Faculty of Navigation, Al. Zjednoczenia 3, 81-345 Gdynia, Poland*

Received 16 September 2005; received in revised form 17 July 2006; accepted 20 July 2006
Available online 28 September 2006

Abstract

The application of spectral finite elements (SFE) to one-dimensional (1D) elastic wave propagation problems is presented. Travelling waves in an isotropic rod and Timoshenko beam have been investigated. The rod has been modelled using 1D SFEs while the beam has been modelled using 1D and 2D SFEs. Numerical results have been compared to those obtained from the classical finite element approach. This comparison highlighted the efficiency of the SFE method. The numerical results have been also verified experimentally. A high degree of accuracy has been observed.
© 2006 Elsevier Ltd. All rights reserved.

1. Introduction

Detection of small fatigue damage is a challenging task for most classical damage detection methods. Techniques for small damage detection require high-frequency excitation signals while conventional modal methods become computationally inefficient. The accuracy of a solved problem depends on spatial finite element discretisation. It is evident that the mesh of finite elements should be very dense to reach high vibration modes because then it is possible to capture effects of wave scattering by structural discontinuities [1]. This leads to large systems of equations even for one-dimensional (1D) structures which solving process is time consuming. On the other hand, on-line structural health monitoring (SHM) systems require short computational time.

A number of numerical algorithms and techniques for elastic wave propagation have been developed over the last few decades. This includes: the finite difference method (FDM) [2,3], the finite element method (FEM) [4,5], the boundary element method (BEM) [6,7], the spectral element method (SEM) [1,8–13], the Mass–spring lattice models (MSLM) [14] and the local interaction simulation approach (LISA) [15]. Modelling of wave interaction with damage has found relatively less attention in the literature. Most applications are related to wave scattering problems using FE-based approaches [16].

*Corresponding author.
E-mail addresses: pk@imp.gda.pl (P. Kudela), mk@imp.gda.pl (M. Krawczuk), wieslaw@imp.gda.pl (W. Ostachowicz).

0022-460X/$ - see front matter © 2006 Elsevier Ltd. All rights reserved.
doi:10.1016/j.jsv.2006.07.031

It is necessary to distinguish two different spectral element approaches reported in the literature. The first one is based on the fast Fourier transformation (FFT) [1,8], whereas the second one is the time domain method [10–13].

Among many frequency domain methods based on FFT, the SEM [8] is potentially the most effective numerical tool for wave propagation modelling. However the FFT-based SEM demands additional throw-off elements due to the periodic nature of the FFT. Because of that Doyle [8] solves only problems of infinite or semi-infinite rods and beams. To overcome the problem of the periodic nature of the FFT the Laplace transform can be applied instead of the FFT [9]. Following the Laplace transform technique 3D frame structures of finite-lengths can be treated practically. In case of FFT-based SEM it is difficult to formulate an adequate model for such complex structures. No results have been reported in the literature related to the windowing feature of the discrete FFT in plate and shell-like structures.

In this paper a study of the second approach as proposed by Patera in 1984 [10] has been carried out. The method is versatile and has found many applications in the field of fluid dynamics, heat transfer, acoustic and for modelling seismic wave propagation. So far the method has been successfully applied to 2D and 3D problems related to elastic, isotropic media as well the method having been extended to fully anisotropic media [11]. Because of the similar nature to the FE it is called the spectral finite element (SFE).

In this paper an efficient and accurate SFE (time domain method) has been applied for detection of waves scattered by discontinuities in 1D structures. However this approach can be easily extended to 2D and 3D problems. Results of numerical analysis obtained have been compared with experimental results and with the classical FE approach.

2. Spectral finite element formulation

The SFE formulation process of the stiffness and mass matrices is analogous to the classical FE formulation. A crucial idea of the SFE method is adoption of specific shape functions. In an element, a set of local shape functions is defined consisting of Lagrange polynomials. Firstly the degree N of the Legendre polynomials [17] has to be chosen. Local nodes $\xi_i \in [-1,1]$, $i \in 1,\ldots,(N+1)$ are obtained as roots of the equation:

$$(1-\xi^2)P'_N(\xi) = 0, \tag{1}$$

where $P'_N(\xi)$ denotes the first derivative of the Legendre polynomial of degree N. The local nodes are defined as Gauss–Lobatto–Legendre (GLL) points. For instance the nodes of an 8-node element have the following nodal coordinates:

$$\xi_1 = -1$$

$$\xi_2 = -0.8717401485096066$$

$$\xi_3 = -0.5917001814331423$$

$$\xi_4 = -0.2092992179024788$$

$$\xi_5 = -\xi_4$$

$$\xi_6 = -\xi_3$$

$$\xi_7 = -\xi_2$$

$$\xi_8 = -\xi_1.$$

For this set of $(N+1)$ nodes Lagrange interpolating polynomials are formulated. The Lagrange interpolating polynomials are the Nth order polynomials that pass through the $(N+1)$ GLL points. In other words, the interior nodes are distributed at positions which correspond to zeros of the orthogonal polynomials. Theoretical analysis shows that in this manner the highest interpolation accuracy is achieved [13]. By definition a Lagrange polynomial is equal to one at $\xi = \xi_i$ and zero at all other points $\xi = \xi_j$ for which $i \neq j$. From this

definition a fundamental property appears:

$$\psi_i(\xi_j) = \delta_{ij}, \tag{2}$$

where δ_{ij} denotes the Kronecker delta and $\psi_i(\xi_j)$ is ith Lagrange interpolant (shape function). The displacement field within the element can be approximated as

$$u_N^e(\xi) = \sum_{i=1}^{N+1} q_N^e(\xi_i)\psi_i(\xi), \tag{3}$$

where $q_N^e(\xi_i)$ denote nodal degrees of freedom. A few examples of shape functions are presented in Fig. 1.

Construction of a weak form (similarly as in the FE approach) element mass and stiffness matrices can be defined [5]. Also boundary conditions must be qualified at this stage. It should be noticed that free boundary conditions at the ends of a spectral element are implemented naturally. Transformation to the global coordinate system and the assembly process are the same as in the FE method. Finally a wave propagation modelling problem is reduced to well-known ordinary differential equations, which can be written in a matrix form:

$$\mathbf{M}\ddot{\mathbf{Q}} + \mathbf{C}\dot{\mathbf{Q}} + \mathbf{K}\mathbf{Q} = \mathbf{F}, \tag{4}$$

where $\mathbf{M}$ is the global mass matrix, $\mathbf{C} = \eta\mathbf{M}$ is the global damping matrix with damping parameter η, $\mathbf{K}$ is the global stiffness matrix, and $\mathbf{F}$ is a vector of the time dependent excitation signal. An element is mapped from the x-axis to the standard interval $\Lambda = [-1, 1]$ of the parametric ξ-axis: $\mathscr{F}_e : \Lambda \to \Omega_e$. The element matrices $\mathbf{M}^e$, $\mathbf{K}^e$ and the column vector $\mathbf{F}^e$ are computed numerically using the GLL integration rule:

$$\mathbf{M}^e = \int_{\Omega_e} (\boldsymbol{\psi}^e(x))^{\mathrm{T}} \boldsymbol{\mu}^e \boldsymbol{\psi}^e(x)\,\mathrm{d}x \approx \sum_{i=1}^{N+1} w_i\,(\boldsymbol{\psi}^e(\xi_i))^{\mathrm{T}} \boldsymbol{\mu}_i^e \boldsymbol{\psi}^e(\xi_i)\ \det(\mathbf{J}^e(\xi_i)), \tag{5}$$

$$\mathbf{K}^e = \int_{\Omega_e} (\mathbf{B}^e(x))^{\mathrm{T}} \mathbf{D}^e \mathbf{B}^e(x)\,\mathrm{d}x \approx \sum_{i=1}^{N+1} w_i\,(\mathbf{B}^e(\xi_i))^{\mathrm{T}} \mathbf{D}_i^e\,\mathbf{B}^e(\xi_i)\ \det\,(\mathbf{J}^e(\xi_i)), \tag{6}$$

$$\mathbf{F}^e = \int_{\Omega_e} (\boldsymbol{\psi}^e(x))^{\mathrm{T}} \mathbf{p}(x)^e\,\mathrm{d}x \approx \sum_{i=1}^{N+1} w_i (\boldsymbol{\psi}^e(\xi_i))^{\mathrm{T}} \mathbf{p}(\xi_i)^e \det(\mathbf{J}^e(\xi_i)), \tag{7}$$

where $\boldsymbol{\mu}^e$ is the mass density per unit length, $\mathbf{D}^e$ is termed material stiffness matrix, $\mathbf{J}^e$ is the Jacobian associated with the mapping $\mathscr{F}_e$ from the element Ω_e to the reference domain Λ and $\mathbf{p}(x)^e$ is a distributed load.

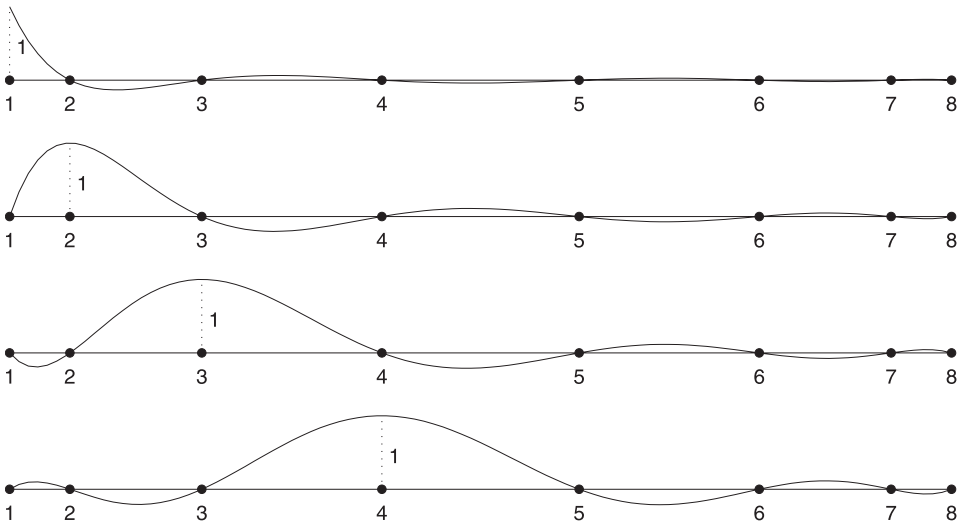

Fig. 1. First four 8-node element's shape functions.

The matrix $\mathbf{B}^e$ is connected with approximated strains:

$$\mathbf{B}^e = \mathbf{L}\,\boldsymbol{\psi}^e(\xi_i), \tag{8}$$

where $\mathbf{L}$ denotes a differential operator matrix.

The quadrature weights $w_i > 0$, which are independent of the element, are determined from:

$$w_i = \frac{2}{n(n-1)[P_{n-1}(\xi_i)]^2}, \quad i \in 1,\ldots,n, \quad n = N+1. \tag{9}$$

As a consequence of the Lagrange interpolants selection at the GLL points in conjunction with the GLL integration rule the following discrete orthogonality (vide Eq. (5)) holds:

$$\sum_{i=1}^{N+1} w_i \psi_n(\xi_i)\psi_m(\xi_i) = \begin{cases} C_n & \text{if } n = m, \\ 0 & \text{if } n \neq m, \end{cases} \tag{10}$$

where C_n are constants. This property is very important for the SFE method because it leads to the *diagonal form of the mass matrix* $\mathbf{M}$, which allows a crucial reduction of the complexity and the cost of the algorithm [12]. In this manner the diagonal mass matrix is obtained naturally in comparison with mass matrix lumping techniques which incorporate significant errors.

In order to take full advantage of the property described above discretisation of the second-order ordinary differential equation in time (4) is achieved using the Newmark scheme (central difference method). The Newmark scheme is of second-order accuracy and is conditionally stable [18]. Zero initial displacements and velocities are assumed in the numerical simulations.

3. Numerical models

In the current analysis three types of elements have been investigated: rod elements, Timoshenko beam elements and 2D solid elements. It has been assumed that the material is homogeneous and isotropic. The proposed elements are examined under assumption of no damping, except the case of the rod.

3.1. An isotropic rod element

The strains within the rod based on the elementary rod theory can be written as

$$\varepsilon_x = \frac{\partial u}{\partial x}. \tag{11}$$

Therefore, the matrix of differential operators related to Eq. (8) is

$$\mathbf{L} = \left[\frac{\partial}{\partial x}\right], \quad \left[\frac{\partial}{\partial x}\right] = \mathbf{J}^{-1}\left[\frac{\partial}{\partial \xi}\right] \tag{12}$$

because the element has one degree of freedom per node (longitudinal displacement). The mass density matrix per unit length from Eq. (5) can be expressed as

$$\boldsymbol{\mu}^e = [\rho A], \tag{13}$$

where ρ is the density, and A the cross-sectional area. The material stiffness matrix from Eq. (6) has the form

$$\mathbf{D}^e = [EA], \tag{14}$$

where E is the Young's modulus.

The stiffness and mass matrices for a 8-node element have been developed using relations stated in the previous section and taking into account Eqs. (12)–(14). The equation of motion (4) includes a damping matrix which is proportional to the mass matrix: $\mathbf{C} = \eta\mathbf{M}$.

3.2. An isotropic Timoshenko beam element

The strains within the beam, based on the Timoshenko theory, can be written as

$$\varepsilon = \begin{bmatrix} \dfrac{\partial u_o}{\partial x} + z\dfrac{\partial \varphi}{\partial x} \\ \dfrac{\partial w}{\partial x} + \varphi \end{bmatrix} = \begin{bmatrix} \varepsilon_o + z\kappa \\ \gamma \end{bmatrix}. \tag{15}$$

Assuming isotropy the strains $\varepsilon_o, \kappa, \gamma$ can be approximated individually. The element has three degrees of freedom per node u_o, w, φ which are shown in Fig. 2. These displacements are approximated using $N = 7$ degrees of the Lagrange polynomials so that the shape function matrix has the form

$$\boldsymbol{\psi} = \begin{bmatrix} \psi_{u_1} & 0 & 0 & \psi_{u_2} & 0 & 0 & \cdots & \psi_{u_8} & 0 & 0 \\ 0 & \psi_{w_1} & 0 & 0 & \psi_{w_2} & 0 & \cdots & 0 & \psi_{w_8} & 0 \\ 0 & 0 & \psi_{\varphi_1} & 0 & 0 & \psi_{\varphi_2} & \cdots & 0 & 0 & \psi_{\varphi_8} \end{bmatrix}, \tag{16}$$

where $\psi_{u_i} = \psi_{w_i} = \psi_{\varphi_i}, i = 1, \ldots, 8$. The matrix of differential operators related to Eq. (8) can be written as

$$\mathbf{L} = \begin{bmatrix} \dfrac{\partial}{\partial x} & 0 & 0 \\ 0 & 0 & \dfrac{\partial}{\partial x} \\ 0 & \dfrac{\partial}{\partial x} & 1 \end{bmatrix}, \quad \begin{bmatrix} \dfrac{\partial}{\partial x} \end{bmatrix} = \mathbf{J}^{-1} \begin{bmatrix} \dfrac{\partial}{\partial \xi} \end{bmatrix}. \tag{17}$$

The mass density matrix per unit length from Eq. (5) is

$$\boldsymbol{\mu}^e = \begin{bmatrix} \rho A & 0 & 0 \\ 0 & \rho A & 0 \\ 0 & 0 & \rho I \end{bmatrix}, \tag{18}$$

where ρ is the density, A the cross-sectional area, and I the moment of inertia. The material stiffness matrix from Eq. (6) has the form

$$\mathbf{D}^e = \begin{bmatrix} EA & 0 & 0 \\ 0 & EI & 0 \\ 0 & 0 & GA \end{bmatrix}, \tag{19}$$

where $G = E/2(1 + \nu)$ is the shear modulus.

The stiffness and mass matrices for a 8-node element have been developed using relations stated in the Section 2 and taking into account Eqs. (15)–(19). The damping parameter η from Eq. (4) has been assumed as being equal to zero.

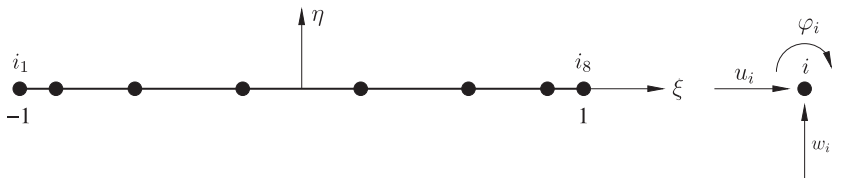

Fig. 2. Scheme of an 8-node beam SFE. Degrees of freedom: horizontal displacement u, vertical displacement w and slope φ.

3.3. An isotropic 2D solid element

The strains within the 2D solid element can be written:

$$\varepsilon = \begin{bmatrix} \dfrac{\partial u}{\partial x} \\ \dfrac{\partial v}{\partial y} \\ \dfrac{\partial u}{\partial y} + \dfrac{\partial v}{\partial x} \end{bmatrix}. \tag{20}$$

The element (Fig. 3) has two degrees of freedom per node: u and v. Two different degrees of the Legendre polynomials have been chosen: 7 in the ξ direction and 2 in the η direction, so that the shape functions are:

$$\boldsymbol{\psi} = \begin{bmatrix} \psi_1 & 0 & \psi_2 & 0 & \cdots & \psi_{24} & 0 \\ 0 & \psi_1 & 0 & \psi_2 & \cdots & 0 & \psi_{24} \end{bmatrix}. \tag{21}$$

The matrix of differential operators related to Eq. (8) can be written:

$$\mathbf{L} = \begin{bmatrix} \dfrac{\partial}{\partial x} & 0 \\ 0 & \dfrac{\partial}{\partial y} \\ \dfrac{\partial}{\partial y} & \dfrac{\partial}{\partial x} \end{bmatrix}, \quad \begin{bmatrix} \dfrac{\partial}{\partial x} \\ \dfrac{\partial}{\partial y} \end{bmatrix} = \mathbf{J}^{-1} \begin{bmatrix} \dfrac{\partial}{\partial \xi} \\ \dfrac{\partial}{\partial \eta} \end{bmatrix}. \tag{22}$$

The mass density matrix per unit length from Eq. (5) has the form

$$\boldsymbol{\mu}^e = \begin{bmatrix} \rho h & 0 \\ 0 & \rho h \end{bmatrix}, \tag{23}$$

where ρ is the density, and h the beam height. The material stiffness matrix from Eq. (6) has the form

$$\mathbf{D}^e = \frac{E}{1-\nu^2} \begin{bmatrix} 1 & \nu & 0 \\ \nu & 1 & 0 \\ 0 & 0 & \dfrac{1-\nu}{2} \end{bmatrix}. \tag{24}$$

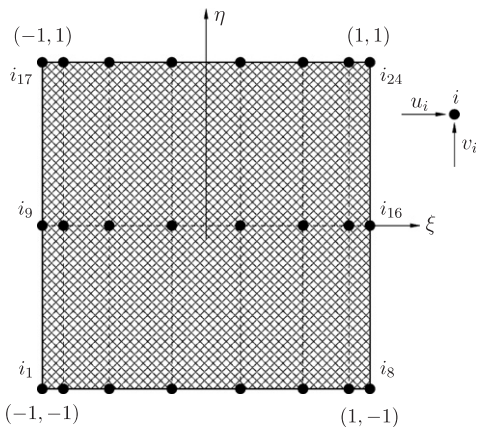

Fig. 3. Scheme of a 24-node 2D solid SFE. Degrees of freedom: horizontal displacement u, vertical displacement v.

The stiffness and mass matrices for a 24-node 2D solid element have been developed using relations stated in Section 2 and taking into account Eqs. (20)–(24). The damping parameter η from Eq. (4) has been assumed as equal to zero.

4. Numerical analysis

4.1. Waves propagating in an aluminium rod

The aim of this section is to verify the developed model of the spectral rod by comparison of numerical results with results obtained from the experiment. An aluminium rod with an additional mass has been investigated numerically and experimentally [19] as presented in Fig. 4. The rod has the cross-sectional dimensions: width 0.01 m, height 0.001 m, and material properties: Young's modulus 70 GPa and mass density 2700 kg/m^3 (the same as in the experiment). The length of the rod is 2 m and is denoted by L; the additional mass is located at a distance L_1 from the left end of the rod. Several numerical tests have been carried out for the rod partially fixed at the left end and free at the right end. The actuation point is located approximately $d \approx 1$ cm from the left end of the rod.

The numerical model is based on 80 SFEs. An excitation signal has been taken to be the same as in the experiment but included only 10,000 sampling points. The excitation signal is a product of a Hanning window multiplied by a sinusoidal signal with frequency 100 kHz (Fig. 5).

Figs. 6 and 7 show a comparisons of two signals obtained from simulation and the experiment. These signals have been obtained for the rod with an additional mass equal to 4% of the total rod mass and have been measured at the left end of the rod. The additional mass has been placed at the middle (Fig. 6), and in two thirds of the rod's length (Fig. 7), respectively. Three peaks of the recorded signal are visible. The first peak corresponds to the excitation, the second one is a reflection from the additional mass, and the last peak is the reflection from right end of the rod.

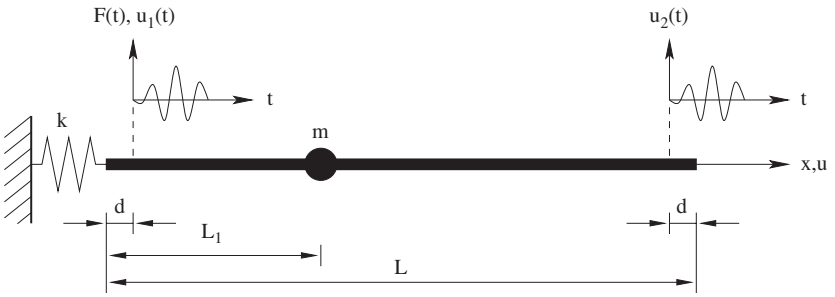

Fig. 4. An aluminium rod with an additional mass.

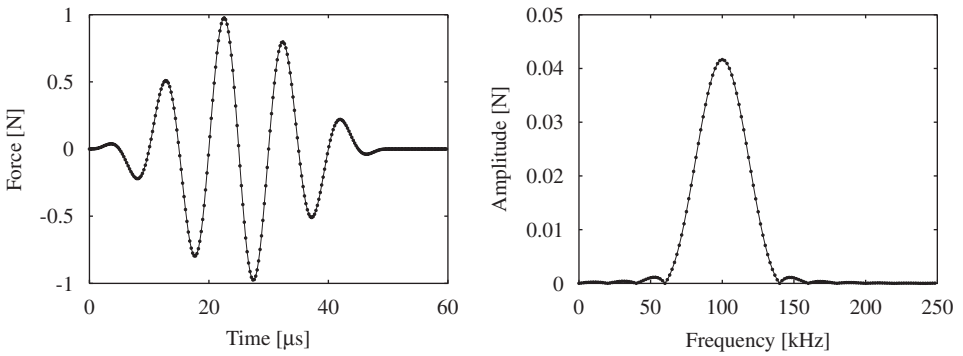

Fig. 5. An excitation signal in time and frequency domains, respectively.

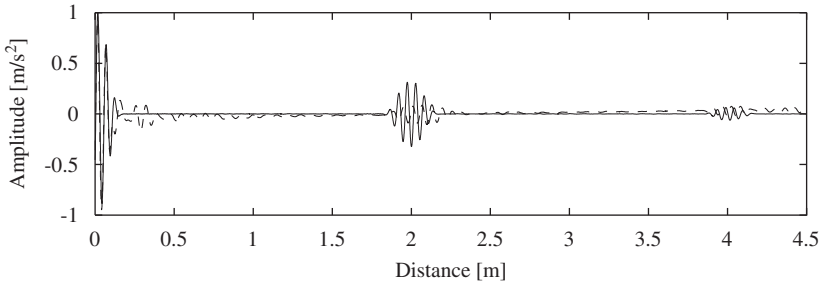

Fig. 6. Wave propagation comparison between simulation (solid line) and experiment (dashed line); 4% additional mass located at 50% of the rod's length.

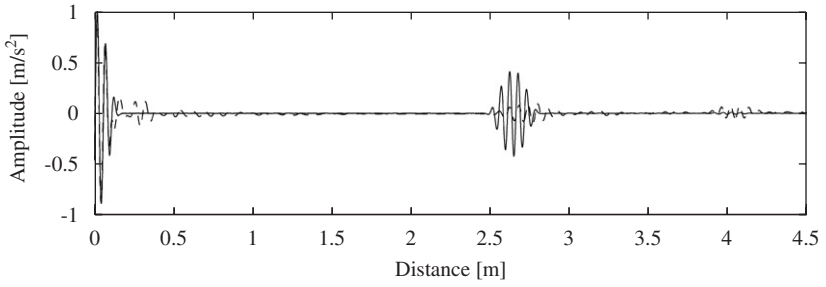

Fig. 7. Wave propagation comparison between simulation (solid line) and experiment (dashed line); 4% additional mass located at 66% of the rod's length.

It is easy to detect the location of the additional mass by taking into account the wave propagation speed and the time interval between the peaks. The known value of wave propagation speed allows one to change the time axis into the distance axis as presented in Figs. 6 and 7. The peak visible in Fig. 6 at the distance of 2 m indicates that a wave travelling along the rod has been reflected at the distance of 1m in order to come again to the left end of the rod.

A good agreement between the calculation and experimental results can be seen except for small disturbances after each reflection seen in the measured signal. It is not possible to select the damping parameter η (see $\mathbf{C} = \eta\mathbf{M}$ in Eq. (4)) such that both the measured and the calculated signal amplitudes have the same level. However, the relationship between the amplitude of the reflected signals (from the additional mass and from the right end of the rod) is the same as in the case of the experimental investigation. This proves the correctness of the numerical model.

In the next example the influence of the magnitude of the additional mass on wave propagation in the rod is investigated. Two different additional masses (2% and 10% of the total rod mass) were considered and placed in the middle of the rod. The curves in Fig. 8a show the results of numerical simulation, whereas the curves in Fig. 8b illustrate the changes in the propagating waves obtained from the experiment. For clarity only the envelopes of the signals obtained are shown.

Fig. 8b shows that an increase in the mass causes a reduction in the reflection signal from the free end, while the reflection from the additional mass is amplified. Similar behaviour is produced by the numerical model by incorporation of the damping parameter η depending on the magnitude of the additional mass, as is presented in Fig. 8a.

An interesting effect is observed in the even distribution of the additional mass along three nodes of the element located at the middle of the rod (Fig. 9). Such small mass distribution (over 3 mm) causes a distortion in the response similar to dispersion. What important is that it is easy to distinguish the magnitude of the additional mass, because the bigger mass results in the greater dispersion. In this case the damping parameters η have been constant irrespective of the magnitude of the additional mass.

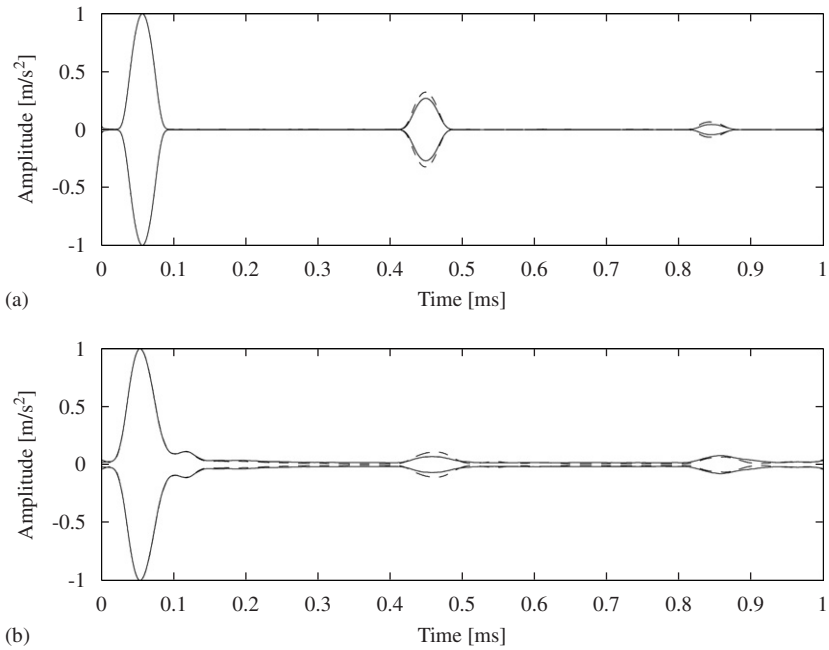

Fig. 8. Comparison between simulated (a) and measured (b) signal envelopes. Dashed line: 10% additional mass, solid line: 2% additional mass.

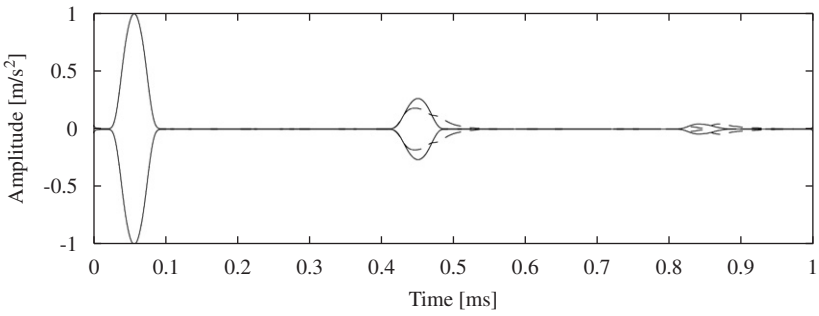

Fig. 9. Signal envelope from numerical data—mass lumped at 3 nodes; Dashed line: 10% additional mass, solid line: 4% additional mass.

4.2. *Waves propagating in an aluminium Timoshenko beam: variant 1*

For the first stage the numerical model is based on 1D beam SFEs (see Fig. 2). Results obtained for a beam modelled by 100 SFEs have been compared with the results obtained from the FE approach. The material properties are taken to be the same as for the rod. The beam has dimensions: width 0.06 m, height 0.06 m, and length 3 m.

The excitation signal is identical with the signal used in Section 4.1 (see Fig. 5). The assumed beam dimensions, material properties and excitation signal frequency results in separation of the second mode which is present in the response signal (Fig. 10). The second mode is obtained because the excitation signal frequency is higher than the cut-off frequency for this mode [8].

In order to compare the signals obtained using SFEs with the signal from the FEs, an 8-node FE with cubic shape functions is developed. Also in this case the element has three degrees of freedom per node and the same number of elements has been taken as in the SFE method. A very good agreement between the SFE and FE both for wave propagation (Fig. 10) and for natural frequencies (Fig. 11) is observed. Moreover, the SFE method is substantially faster than the FE method, because of diagonal mass matrix property. Calculation

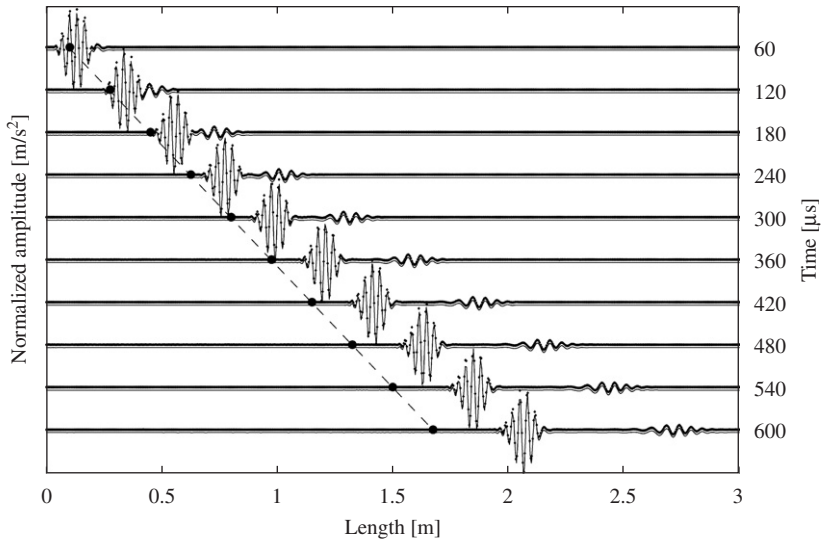

Fig. 10. Comparison between vertical accelerations for: SFE (solid line) and FE (◆ ◆ ◆) showing the presence of the second propagating mode. Theoretical wave front of the first mode is marked by the dashed line.

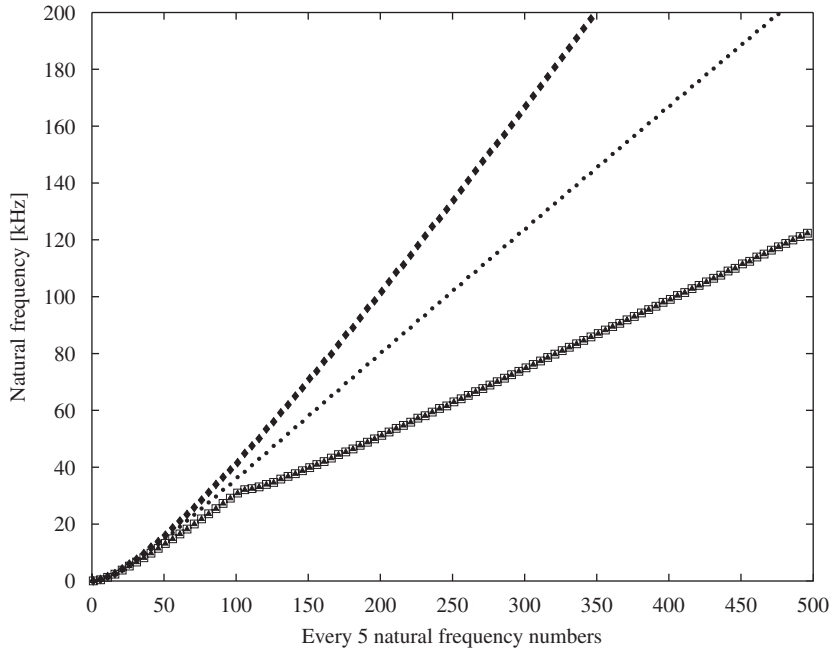

Fig. 11. Comparison between natural frequencies for simply supported beam; ◆ beam without transverse shear deformation effects (theory), • beam with transverse shear deformation effects (theory), ▲ 100 FEs, □ 100 SFEs.

time depends on the implementation of the algorithm used for solution of the equation of motion, but numerical tests discussed in this paper show that the SFE method needs less time than the time required by FE method.

Another remark is that for both considered methods the first wave in Fig. 10 travel too fast comparing with theoretical speed [8]. Theoretical group wave speed connected with the centre of the wave packet give a function which has been marked in Fig. 10 by dashed line with dots. The conclusion is that more accurate model should be applied.

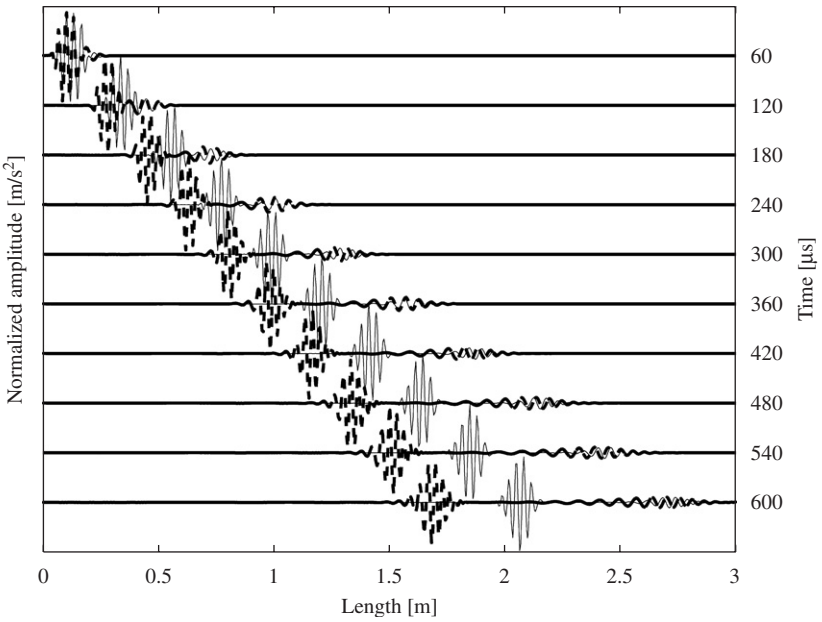

Fig. 12. Comparison between 1D and 2D *variants*. Solid line—1D case, dashed line—2D case with accelerations on upper edge of the beam.

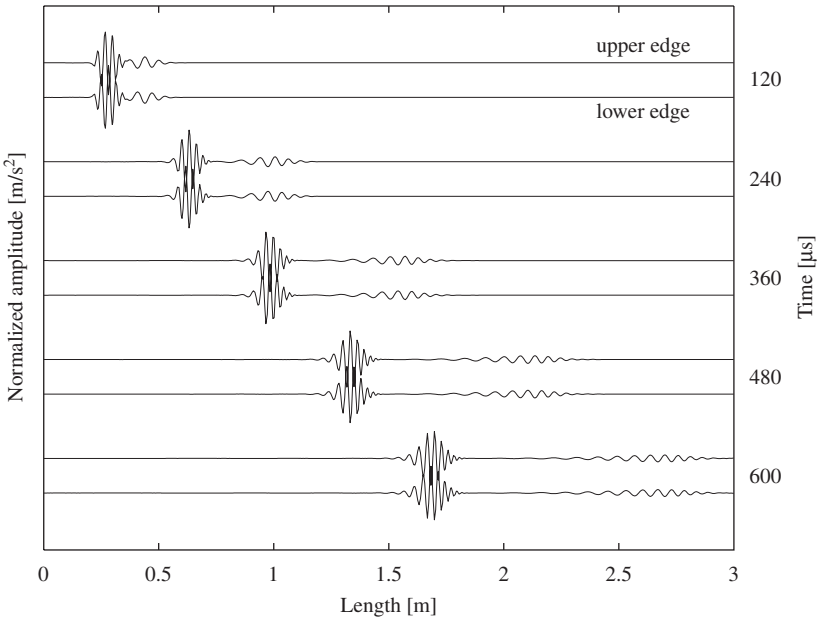

Fig. 13. Symmetric modes. Couple of the accelerations on the upper and lower edge of the beam.

4.3. *Waves propagating in an aluminium Timoshenko beam: variant 2*

In this example the beam modelled by 2D solid SFEs is investigated. The same parameters as in the model based on 1D beam SFEs have been used. The modelled beam is composed of 100 2D solid SFEs (see Fig. 3) connected in such a manner that they build up into one layer.

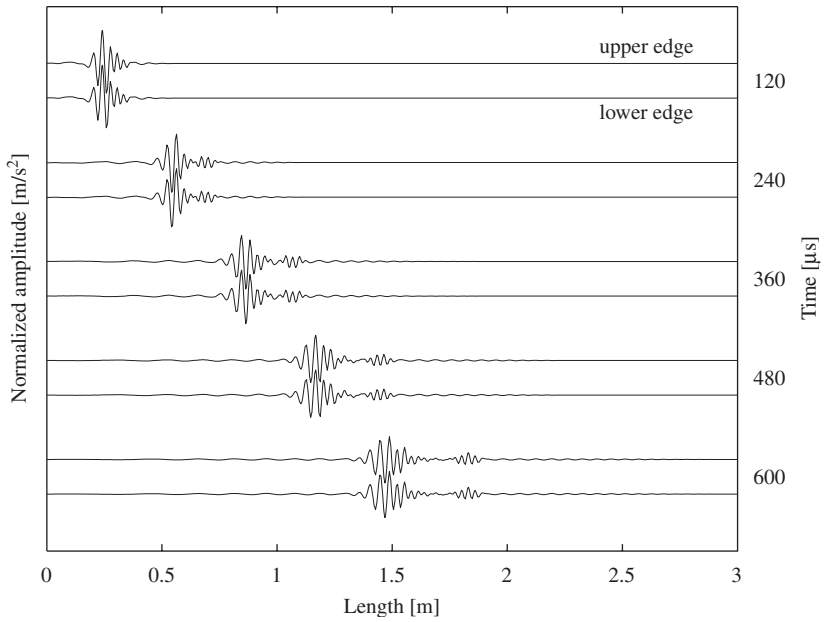

Fig. 14. Anti-symmetric modes. Couple of the accelerations on the upper and lower edge of the beam.

Fig. 12 shows the comparison between two different modelling techniques in which 1D and 2D SFEs are used. In the case of 2D solid elements the first mode travels with proper speed. The second mode is present at the same position for both cases but 2D solid elements produce more dispersion.

The symmetrical (S) or anti-symmetrical (A) modes are excited by applying simultaneously normal forces on the upper and lower surfaces of the beam in opposite (S) or the same (A) directions, respectively. As one can expect the S0 and S1 modes (Fig. 13) travel faster and are associated with longitudinal vibration, and the A0 and A1 modes (Fig. 14) travel more slowly and are associated with flexural vibration.

5. Conclusions

Physical understanding of wave propagation phenomena in structures can be significantly helpful in damage detection. This paper has presented several aspects of elastic waves propagation behaviour, especially concerned with the detection of small damage. In this case, only simple examples of a rod with an additional mass have been shown. Comparison between the experimental and numerical results confirms that the considered SFE method reflects this phenomenon quite well. Other examples presented in this work prove that the investigated SFEs are efficient and accurate. Moreover, examples given in the work enables one to make a few final statements:

- It has been found that the location of the additional mass in the rod can be detected by considering the wave speed and the time of reflection appearance in response signal. Also the magnitude of the additional mass can be identified by considering the signal envelope.
- The method presented is very efficient in comparison with the classical FE method, calculation time is substantially shorter (approximately 50%). It is the effect of a very fast direct time integration algorithm adjusted to take full advantage of the diagonal mass matrix property.
- A 2D model of the beam gives better results than the 1D model. A high-frequency excitation signal produces the second mode which is present in the signal response in the 1D model and the 2D model as well. However, only in the 2D model do the waves propagate with a proper speed.
- In the 2D model the physical behaviour corresponding to the propagation of Lamb waves is also captured. In the 1D model it is necessary to consider longitudinal and shear waves separately.

Future research will be focused on the development of cracked SFEs based on fracture mechanics laws and also these elements will consider material anisotrophy. The SFE approach will be also extended to damaged structures with more complex geometry, like curved beams, plates, shells or 3D structures.

Acknowledgements

The authors of this work would like to gratefully acknowledge the support for this research provided by the EU under the Sixth EU Framework Programme for Research and Technological Development (FP6) via the ARTIMA project (Aircraft Reliability Through Intelligent Materials Application—reference number 502725), as well as wishing to thank the Polish Ministry of Scientific Research and Information Technology.

References

[1] M. Palacz, M. Krawczuk, W. Ostachowicz, The spectral finite element model for analysis of flexural-shear coupled wave propagation, Part 1: laminated multilayer composite, *Composite Structures* 68 (2005) 37–44.
[2] B. Hackbush, *Multi-Grid Methods and Applications*, Springer, Berlin, 1985.
[3] J. Orkisz, Finite difference method (Part III), *Handbook of Computational Solid Mechanics*, Springer, Berlin, 1998, 336–432.
[4] O.C. Zienkiewicz, *The Finite Element Method*, fourth ed., McGraw-Hill, London, 1989.
[5] J.N. Reddy, *An Introduction to the Finite Element Method*, second ed., Engineering Mechanics Series, McGraw-Hill International Editions, Singapore, 1993.
[6] C.A. Brebbia, J.C.F. Tells, L.C. Wrobel, *Boundary Elements Techniques*, Springer, Berlin, 1984.
[7] Y. Cho, J.L. Rose, A boundary element solution for mode conversion study of the edge reflection of lamb waves, *Journal of the Acoustical Society of America* 99 (1996) 2079–2109.
[8] J.F. Doyle, *Wave Propagation in Structures*, Springer, New York, 1997.
[9] H. Igawa, K. Komatsu, I. Yamaguchi, T. Kasai, Wave propagation analysis of frame structures using the spectral element method, *Journal of Sound and Vibration* 277 (2004) 1071–1081.
[10] A.T. Patera, A spectral element method for fluid dynamics: laminar flow in a channel expansion, *Journal of Computational Physics* 54 (1984) 468–488.
[11] D. Komatitsch, Ch. Barnes, J. Tromp, Simulation of anisotropic wave propagation based upon a spectral element method, *Geophysics* 4 (2000) 1251–1260.
[12] D. Komatitsch, R. Martin, J. Tromp, M.A. Taylor, B.A. Wingate, Wave propagation in 2-D elastic media using a spectral element method with triangles and quadrangles, *Journal of Computational Acoustics* 9 (2) (2001) 703–718.
[13] C. Pozrikidis, *Introduction to Finite and Spectral Element Methods Using MATLAB®*, San Diego, USA, 2005.
[14] P.P. Delsanto, R.B. Mignogna, A spring model for the simulation of the ultrasonic pulses through imperfect contact interfaces, *Journal of Acoustical Society of America* 104 (1998) 1–8.
[15] P.P. Delsanto, T. Whitecomb, H.H. Chaskelis, R.B. Mignogna, Connection machine simulation of ultrasonic wave propagation in materials. I: the one-dimensional case, *Wave Motion* 16 (1992) 65–80.
[16] W.J. Staszewski, Ultrasonic/guided waves for structural health monitoring, *Key Engineering Materials*, vols. 293–294, Trans Tech Publications, September 2005, pp. 49–60.
[17] http://mathworld.wolfram.com/LegendrePolynomial.html.
[18] M. Kleiber, *Finite Element Method in Non-linear Continuum Mechanics*, Warsaw, 1985
[19] M. Palacz, M. Krawczuk, W. Ostachowicz, Detection of additional mass in rods: experimental and numerical investigation, *Archive of Applied Mechanics* (2005) (Published online).